

Acute SARS-CoV-2 Infection is Highly Cytopathic, Elicits a Robust Innate Immune Response and is Efficiently Prevented by EIDD-2801

Angela Wahl^{1,2,3*}, Lisa E. Gralinski^{4*}, Claire E. Johnson^{1,2,3}, Wenbo Yao^{1,2,3}, Martina Kovarova^{1,2,3}, Kenneth H. Dinno III^{4,5}, Hongwei Liu^{6,7}, Victoria J. Madden⁸, Halina M. Krzystek^{6,7}, Chandrav De^{1,2,3}, Kristen K. White⁸, Alexandra Schäfer⁴, Tanzila Zaman^{6,7}, Sarah R. Leist⁴, Paul O. Grant^{6,7}, Kendra Gully⁴, Frederic B. Askin⁹, Edward P. Browne^{2,3,5,10}, Corbin D. Jones^{6,7}, Raymond J. Pickles^{5,11}, Ralph S. Baric^{4,5,12}, J. Victor Garcia^{1,2,3†}

¹International Center for the Advancement of Translational Science, University of North Carolina at Chapel Hill, Chapel Hill, NC, USA

²Division of Infectious Diseases, Department of Medicine, University of North Carolina at Chapel Hill, Chapel Hill, NC, USA

³Center for AIDS Research, University of North Carolina at Chapel Hill, Chapel Hill, NC, USA

⁴Department of Epidemiology, University of North Carolina at Chapel Hill, Chapel Hill, NC, USA

⁵Department of Microbiology and Immunology, University of North Carolina at Chapel Hill, Chapel Hill, NC, USA.

⁶Department of Biology, University of North Carolina at Chapel Hill, Chapel Hill, NC, USA

⁷Department of Genetics, University of North Carolina at Chapel Hill, Chapel Hill, NC, USA

⁸Microscopy Services Laboratory, University of North Carolina at Chapel Hill, Chapel Hill, NC, USA

⁹Department of Pathology, University of North Carolina at Chapel Hill, Chapel Hill, NC, USA

¹⁰UNC HIV Cure Center, University of North Carolina at Chapel Hill, Chapel Hill, NC, USA

¹¹Marsico Lung Institute, University of North Carolina, Chapel Hill, NC, USA

¹²Rapidly Emerging Antiviral Drug Discovery Initiative, University of North Carolina, Chapel Hill, NC, USA

*These authors contributed equally to this work.

†Corresponding author. Email: victor_garcia@med.unc.edu

Summary Paragraph

All known recently emerged human coronaviruses likely originated in bats. Here, we used a single experimental platform based on human lung-only mice (LoM) to demonstrate efficient *in vivo* replication of all recently emerged human coronaviruses (SARS-CoV, MERS-CoV, SARS-CoV-2) and two highly relevant endogenous pre-pandemic SARS-like bat coronaviruses. Virus replication in this model occurs in bona fide human lung tissue and does not require any type of adaptation of the virus or the host. Our results indicate that bats harbor endogenous coronaviruses capable of direct transmission into humans. Further detailed analysis of pandemic SARS-CoV-2 *in vivo* infection of LoM human lung tissue showed predominant infection of human lung epithelial cells, including type II pneumocytes present in alveoli and ciliated airway cells. Acute SARS-CoV-2 infection was highly cytopathic and induced a robust and sustained Type I interferon and inflammatory cytokine/chemokine response. Finally, we evaluated a pre-exposure prophylaxis strategy for coronavirus infection. Our results show that prophylactic administration of EIDD-2801, an oral broad spectrum antiviral currently in phase II clinical trials for the treatment of

COVID-19, dramatically prevented SARS-CoV-2 infection *in vivo* and thus has significant potential for the prevention and treatment of COVID-19.

Main Text

The recently emerged human pandemic coronavirus Severe Acute Respiratory Syndrome coronavirus-2 (SARS-CoV-2), the causative agent of coronavirus disease (COVID)-19, has spread to six continents resulting in substantial morbidity and mortality worldwide¹. Bats serve as a natural reservoir for coronaviruses and are the presumed source of SARS-CoV-2 and the highly pathogenic human coronaviruses SARS-CoV and Middle East Respiratory Syndrome (MERS)-CoV². Transmission of coronaviruses from bats to other species is well-documented and adaptation in an intermediary host can facilitate their transmission to humans². While it is possible that SARS-CoV-2 was transmitted to humans via an intermediate host such as pangolins, phylogenic analysis indicates that the SARS-CoV-2 lineage has circulated in bats for decades and evolved in bats into a virus capable of replicating in human cells³. Thus, bats are a potential reservoir for coronaviruses with human pandemic potential that can be directly transmitted to humans. Given the repeated and accelerating emergence of highly pathogenic coronaviruses, it has become increasingly important to monitor and characterize coronaviruses circulating in bats and to identify the viral determinants of human infection, disease, and global spread as well as to develop effective therapeutic interventions. Animal models are useful in studying highly pathogenic human coronaviruses, the emergence potential of zoonotic coronaviruses, and to evaluate novel inhibitors for their ability to control coronavirus infection⁴⁻¹⁵. However, human coronaviruses do not replicate in mice without either extensive adaptation of the virus or genetic modification of the host by genetic editing of the receptor or by introducing

the individual human receptor genes for each virus^{4-11,14,15}. Although existing rodent models have made several important contributions to our understanding of coronavirus infection and pathogenesis, none of these models possess the diverse set of primary human cells present in the human lung that can serve as targets for viral infection¹⁶. Here, we show that human lung-only mice (LoM), immune deficient mice implanted with authentic human lung tissue¹⁷, allow for the *in vivo* study of all recently emerged human coronaviruses (SARS-CoV, MERS-CoV, SARS-CoV-2) in a single platform that permits direct comparison of experimental outcomes. Using LoM, we also established that bats harbor novel coronaviruses capable of efficient replication in human lungs without prior adaptation. In addition, we performed an in-depth *in vivo* analysis of acute SARS-CoV-2 infection in the human lung. Our results revealed robust SARS-CoV-2 replication, pathogenesis and sustained activation of the innate host immune response. Finally, we used this platform for the *in vivo* evaluation of EIDD-2801, an orally administered broad spectrum antiviral currently in phase II clinical trials for COVID-19 treatment, to prevent SARS-CoV-2 infection. Our results show that EIDD-2801 efficiently prevented SARS-CoV-2 infection *in vivo* strongly supporting its progression in clinical development for COVID-19.

Human and bat coronavirus replication in LoM

LoM are constructed by subcutaneous implantation of a small piece of human lung tissue into the back of immune deficient mice (Fig. 1a). Previously, we demonstrated that the human lung tissue expands to form a highly vascularized palpable implant¹⁷ (Fig. 1a). These lung implants contain human fibroblast, epithelial, endothelial, and mesenchymal cells that form highly relevant lung structures including cartilaginous and non-cartilaginous bronchial airways lined with ciliated and non-ciliated epithelium, alveolar sac structures, and extensive vasculature¹⁷(Extended Data Fig.

1a,b). We also showed that the human lung tissue of LoMs supports replication of a diverse set of emerging and clinically relevant human pathogens including Zika virus, human cytomegalovirus, respiratory syncytial virus and MERS-CoV¹⁷. Recently emerged human coronaviruses have used at least two different receptors to gain entry into host cells, human angiotensin converting enzyme-2 (ACE2) and dipeptidyl peptidase 4 (DPP4). SARS-CoV and SARS-CoV-2 use human ACE2 as a receptor while MERS-CoV uses DPP4¹⁸⁻²². These differences in receptor usage influence viral tropism, pathogenesis and disease progression²³. Infection of LoM with MERS-CoV resulted in robust virus replication and infection of human epithelial, endothelial and mesenchymal cells *in vivo*¹⁷. These findings were consistent with the broad cellular distribution of its receptor, DPP4²⁴.

Here, we first evaluated the potential of LoM to serve as a single platform to study all known recently emerged human coronaviruses and the potential of endogenous bat coronaviruses for human emergence. We first confirmed that ACE2, the receptor for SARS-CoV and SARS-CoV-2 in human cells, was present on the surface of human epithelial cells (cytokeratin 19+) in the human lung tissues of LoM (Extended Data Fig. 1c,d). Next, LoM were inoculated with recently emerged coronaviruses SARS-CoV, MERS-CoV, or SARS-CoV-2 (Extended Data Table 1). LoM supported replication of all these viruses *in vivo*. Specifically, SARS-CoV and SARS-CoV-2 infection resulted in mean virus titers of 1.76×10^8 and 2.42×10^7 PFU/g respectively at 2 days post-infection (Fig. 1b). Viral nucleoprotein antigen was abundantly observed in the human lung tissues of SARS-CoV and SARS-CoV-2 infected LoM (Extended Data Fig. 2a). Consistent with our previous results¹⁷, we also observed robust replication of MERS-CoV in the human lung

tissues of LoM with mean titers of 4.79×10^8 PFU/g in LoM human lung tissues at 2 days post-infection (Fig. 1b) and abundant viral antigen (Extended Data Fig. 2a).

Pre-pandemic bat coronaviruses WIV1-CoV and SHC014-CoV have high sequence homology to SARS-CoV, use ACE2 to infect human cells, and grow modestly in primary human airway cultures on liquid interface^{4,5}. LoM were inoculated with WIV1-CoV or SHC014-CoV and virus titers in human lung tissues measured 2 days post-infection (Extended Data Table 1). WIV1-CoV and SHC014-CoV efficiently replicated in the human lung tissue of LoM with mean titers of 1.58×10^7 and 1.48×10^7 PFU/g, respectively (Fig. 1b) and viral antigen was readily detected in human lung tissues (Extended Data Fig. 2b). Collectively, these results demonstrate that LoM serve as single platform where all newly emerged coronaviruses SARS-CoV, MERS-CoV, and SARS-CoV-2 replicated efficiently in human lung tissue. Importantly, the fact that SARS-like bat coronaviruses WIV1-CoV and SHC014-CoV also replicated efficiently in the LoM platform indicates that bats harbor coronaviruses that are potentially capable of direct transmission to humans, thus bypassing the need for further adaptation in an intermediary host.

SARS-CoV-2 replication in LoM

Given the state of the current COVID-19 pandemic and the urgent need to develop therapeutic and preventative approaches to control and prevent infection, we evaluated replication of SARS-CoV-2 in LoM in detail. Human lung tissues of LoM were inoculated with SARS-CoV-2 and titers of replication competent virus determined 2, 6, and 14 days post-exposure (Fig. 1c, Extended Data Table 2). High titers of replication competent virus were noted at all time points although they were highest 2 days post-infection (Fig. 1d). The distribution of virus-infected

cells was determined with RNAscope (viral RNA) and immunofluorescence microscopy (viral nucleoprotein). Virus infection was widely distributed throughout the tissue with large numbers of cells positive for viral RNA (Fig. 1e) and nucleoprotein (Fig. 1f). Co-staining with a human cytokeratin 19 antibody demonstrated that SARS-CoV-2 predominantly infects human epithelial cells in the lung (Fig. 1g). Viral antigen was not detected in human CD34 expressing (endothelial) cells, and only a few human vimentin expressing (mesenchymal) cells were positive for viral nucleoprotein (Fig. 1g). To identify the epithelial cell types in the lung tissue that are susceptible to SARS-CoV-2 infection, we further identified infected cells by assessing co-localization of viral nucleoprotein with antibodies against acetylated alpha-tubulin IV (ciliated cells), CC10 (club cells), HT1-56 (alveolar type I [AT1] pneumocytes), and pro-SP-C (alveolar type II [AT2] pneumocytes) (Fig. 1h). We were able to clearly identify virus antigen in cells which expressed pro-SP-C or acetylated alpha-tubulin IV; we did not detect virus antigen in HT1-56 or CC10 positive cells (Fig. 1h). These results demonstrate that SARS-CoV-2 has limited tropism in the lung with AT2 pneumocytes and ciliated airway epithelial cells being the predominant lung cells infected by virus.

SARS-CoV-2 pathogenesis in LoM

To evaluate the cytopathogenic effects of SARS-CoV-2 during acute infection of human lung tissue in LoM, we used a combination of histological analysis and electron microscopy. Histopathologic analysis revealed several features of early diffuse alveolar damage that have been described in lung tissues of COVID-19 patients including the accumulation of proteinaceous exudate and fibrin in alveolar spaces, desquamation of pneumocytes, multinucleated cell formation, and the appearance of fibrin thrombi in small vessels (Fig. 2)²⁵⁻²⁷.

Proteinaceous exudate, including large globules of protein material, was observed in alveolar spaces, which overlapped with areas of virus accumulation (Fig. 2a,b). As early as 2 days post-infection, desquamation of pneumocytes was also noted; there were a large number of virally infected cells fully detached or detaching from the alveolar basement membrane into the alveolar space (Fig. 2c,d). Infected multi-nucleated cells were also observed (Fig. 2c). While the formation of hyaline membranes was not noted, fibrin was detected in alveolar spaces (Fig. 2e). Importantly, we observed multiple occluded vessels containing fibrin thrombi as reported in the lungs of COVID-19 patients (Fig. 2f,g)²⁵⁻²⁷. Electron microscopy demonstrated the normal architecture and integrity of uninfected AT2 pneumocytes that were present in human lung tissue obtained from LoM two days post-infection (Fig. 2h). In contrast, AT2 cells containing virus particles in the same sample had swollen mitochondria with loss of matrix and cristae as well as rough endoplasmic reticula with distended cisternae, protein accumulation, and virus particles (Fig. 2i). Degenerative SARS-CoV-2 infected AT2 cells detached from the alveolar basal membrane could also be observed in the alveolar luminal space (Fig. 2j). Higher magnification revealed subcellular accumulation of virus containing vesicles indicative of virus replication and egress. Virions with electron dense nucleocapsids and distinctive crown-like spikes were observed (Fig. 2i,j). Consistent with previous reports in human airway epithelial cell cultures and port-mortem lung samples^{26,28}, virions produced by human lung cells were pleomorphic in size (69 to 112 nm) and shape. Despite the extensive damage inflicted in the lung tissue by the virus, the endothelium in the majority of blood vessels was intact with tight junctions, numerous pinocytotic vesicles, and normal mitochondria and endoplasmic reticulum (Fig. 2k,l). Virions were not detected within endothelial cells in agreement with a lack of infection as per our immunofluorescence analysis (Fig. 1g and Fig. 2k,l). However, pleomorphic virions were present

in capillary lumen surrounded by fibrillar protein deposits and cell debris (Fig. 2k,l). Together, these results demonstrate that acute SARS-CoV-2 infection of LoM closely resembles infection of human lung in humans and is highly cytopathic resulting in significant injury to the fragile alveolar lung structures.

To determine the effect of SARS-CoV-2 infection on human gene transcription, we performed RNA-sequencing analysis of human lung tissues collected from animals 2, 6 and 14 days post-infection. Abundant viral transcripts were detected in infected lung tissue, ranging from 0.55% to 3.6% of the total reads at 2 days post-infection (Extended Data Table 3). Viral transcripts were still abundant but lower at 6 days and 14 days post-infection (Extended Data 3). Sequencing data was consistent with previously identified canonical SARS-CoV-2 transcripts²⁹ and confirmed maintenance of the furin cleavage site throughout the course of infection *in vivo*. Analysis of human gene transcripts revealed 1,504 differentially expressed cellular genes between naïve and infected human lung tissue at 2 days post-exposure, the peak of infection (Fig. 3a, Supplementary Tables 1 and 2) (adjusted p value <0.05 after correcting for multiple testing). Of these, 1,043 genes were up-regulated and 461 genes were down regulated in the infected human lung tissue relative to non-infected lung tissue (Fig. 3a, Supplementary Tables 1 and 2). Notably, numerous interferon-stimulated genes (ISGs) and inflammatory cytokine genes, including pro-inflammatory cytokines genes *IL6*, *CXCL8* (IL-8), *CXCL10* (IP-10), *TNF*, and *CCL5* (RANTES) were potently induced in infected lung tissue (Supplementary Tables 1 and 2). We also observed dramatic upregulation of *IFNB1* expression (>1,000 fold) at 2 days post-exposure, suggesting that this cytokine plays a key role in the antiviral response to SARS-CoV-2 (Supplementary Tables 1 and 2). Gene set enrichment analysis (GSEA) showed over 840 gene

pathways significantly upregulated ($p < 0.05$) including response to type 1 interferon ($p = 0.0011$), response to virus ($p = 0.0010$), innate immune response ($p = 0.0010$), cytokine mediated signaling ($p = 0.0010$), cytokine production ($p = 0.0010$), response to stress ($p = 0.0010$), inflammatory response, ($p = 0.0010$), NIK NF-KB signaling ($p = 0.0011$), acute inflammatory response ($p = 0.0035$), regulation of cell death ($p = 0.0030$), and coagulation pathways ($p = 0.0453$) (Fig. 3b). Complement activation, which contributes to SARS-CoV pathogenesis in mouse models¹⁴, was also increased ($p = 0.0470$) (Fig. 3b). Importantly, analysis of host gene expression at later time points demonstrated a sustained upregulation of antiviral and inflammatory genes that in some instances (e.g. *ISG15*, *IFITM1*, *TNF*, *CXCL9*) persisted for up to 14 days post-infection (last time analyzed) (Fig. 3c,d, Extended Data Table 4, Supplementary Tables 1 and 2). These results demonstrate that acute SARS-CoV-2 infection causes a potent and sustained upregulation of innate immune responses in virus-infected human lung tissue.

EIDD-2801 pre-exposure prophylaxis

Currently, there is no vaccine to prevent SARS-CoV-2 infection or effective therapy to treat patients with COVID-19. The ribonucleoside analog β -D-N⁴-hydroxycytidine (NHC) has been shown to broadly inhibit coronavirus infection *in vitro* in human airway epithelial cell cultures, with potent activity against SARS-CoV-2 as well as SARS-CoV, MERS-CoV, and bat SARS-like and MERS-like coronaviruses⁷. We therefore tested the ability of prophylactic EIDD-2801 (also known as MK-4482), the oral pro-drug of NHC, to inhibit SARS-CoV-2 replication *in vivo*. For this purpose, LoM were administered EIDD-2801 starting 12 h prior to SARS-CoV-2 exposure and every 12 h thereafter (Fig. 4a, Extended Data Table 5). Our results show that EIDD-2801 had a dramatic effect on virus infection, significantly reducing the number of

infectious particles in the human lung tissue of EIDD-2801 treated animals in two independent experiments (Fig. 4b,c) by over 100,000 fold (Fig. 4c,d). Furthermore, in contrast to EIDD-2801 treated mice, abundant cell debris and nucleoprotein positive cells could be readily observed in the alveolar lumen of vehicle control treated mice consistent with the extensive pathogenic effects inflicted on the lung by SARS-CoV-2 (Fig. 4e,f). These results demonstrate that prophylactic administration EIDD-2801 is highly effective at preventing SARS-CoV-2 infection and pathogenesis *in vivo*.

Discussion

The zoonotic transmission of the pathogenic SARS-CoV-2 resulted in a pandemic that has inflicted significant morbidity and mortality as well as dire world-wide economic and social consequences. Herein, we describe a unique model for the *in vivo* study of human coronavirus infection particularly well suited to model distal human lung virus infection. Our results demonstrate replication of all known recently emerged human coronaviruses in LoM. Importantly, our results demonstrate that WIV1-CoV and SHC014-CoV, two pre-pandemic endogenous bat viruses can replicate relatively efficiently in LoMs suggesting that coronaviruses circulating in bats have future pandemic potential without the need for further adaptation to the human host. We also show that acute SARS-CoV-2 infection of LoM resulted in significant lung injury and exhibited key features of the extensive pathology observed in lung tissues obtained from patients with severe SARS-CoV-2 infection, including desquamation of alveolar epithelial cells, multi-nucleated cell formation, and fibrin thrombi^{25,27,30,31}. In agreement with analyses of bronchoalveolar fluid obtained from COVID-19 patients and post-mortem patient lung samples^{12,32}, we also observed a significant increase in multiple ISGs in SARS-CoV-2 infected

human lung tissue of LoM. In addition, we observed a robust induction in IFNB1 gene expression in human lung tissue early during acute infection followed by a decline in expression. Interestingly, an analysis of post-mortem COVID-19 patient lungs¹² did not reveal increased IFNB1 expression and it has been shown *in vitro* that its expression is blocked during SARS-CoV infection^{33,34}. These results suggest that in human lung tissue IFNB1 gene expression is induced during the acute phase of SARS-CoV-2 infection. We also observed increased expression of several human cytokine genes in LoM infected with SARS-CoV-2. A substantial number of these cytokines were also increased in the serum of COVID-19 patients and post-mortem lung tissue samples further establishing the similarities between LoM and human infection with SARS-CoV-2^{12,35}. Currently, there is no vaccine to prevent or therapeutics to treat COVID-19. Pre-exposure prophylaxis approaches to infectious diseases have proven to be highly efficacious and can contribute to reduce the risk of infection. The continued global spread of the virus and its associated morbidity and mortality are strong incentives to the development of prevention strategies for COVID-19. In this regard, NHC was shown to have broad activity against human and bat coronavirus infection *in vitro*⁷. In addition, prophylactic and therapeutic administration of its oral pro-drug EIDD-2801 reduced SARS-CoV and MERS-CoV replication and pathogenesis in mice⁷. Here we show that prophylactic administration of EIDD-2801 efficiently prevents SARS-CoV-2 infection *in vivo* highlighting its potential utility as an effective prophylactic agent against SARS-CoV-2 and other past and future zoonotic coronaviruses. There are some limitations of our study including the fact that LoM do not possess the human nasal airway structures that are thought to be early sites of SARS-CoV-2 replication in humans³⁶. Since LoM do not have an autologous human adaptive immune system they reflect the direct effect of viruses on their targets and bystander cells as well as their innate

immune response to infection. Collectively, our results indicate that LoM reflect the pathogenic effects inflicted by SARS-CoV-2 on the human lung and demonstrate their utility as a single *in vivo* platform to evaluate and compare the replication and pathogenesis of past, present, and future pre-emergent, epidemic, and pandemic coronaviruses accelerating the development and testing of pre-exposure prophylaxis agents such as EIDD-2801.

Main References

- 1 Dong, E., Du, H. & Gardner, L. An interactive web-based dashboard to track COVID-19 in real time. *Lancet Infect Dis* **20**, 533-534, doi:10.1016/S1473-3099(20)30120-1 (2020).
- 2 Cui, J., Li, F. & Shi, Z. L. Origin and evolution of pathogenic coronaviruses. *Nat Rev Microbiol* **17**, 181-192, doi:10.1038/s41579-018-0118-9 (2019).
- 3 Boni, M. F. *et al.* Evolutionary origins of the SARS-CoV-2 sarbecovirus lineage responsible for the COVID-19 pandemic. *Nat Microbiol*, doi:10.1038/s41564-020-0771-4 (2020).
- 4 Menachery, V. D. *et al.* SARS-like WIV1-CoV poised for human emergence. *Proc Natl Acad Sci U S A* **113**, 3048-3053, doi:10.1073/pnas.1517719113 (2016).
- 5 Menachery, V. D. *et al.* A SARS-like cluster of circulating bat coronaviruses shows potential for human emergence. *Nat Med* **21**, 1508-1513, doi:10.1038/nm.3985 (2015).
- 6 Jiang, R. D. *et al.* Pathogenesis of SARS-CoV-2 in Transgenic Mice Expressing Human Angiotensin-Converting Enzyme 2. *Cell*, doi:10.1016/j.cell.2020.05.027 (2020).
- 7 Sheahan, T. P. *et al.* An orally bioavailable broad-spectrum antiviral inhibits SARS-CoV-2 in human airway epithelial cell cultures and multiple coronaviruses in mice. *Sci Transl Med* **12**, doi:10.1126/scitranslmed.abb5883 (2020).

299 8 Menachery, V. D. *et al.* Middle East Respiratory Syndrome Coronavirus Nonstructural
300 Protein 16 Is Necessary for Interferon Resistance and Viral Pathogenesis. *mSphere* **2**,
301 doi:10.1128/mSphere.00346-17 (2017).

302 9 Cockrell, A. S. *et al.* A mouse model for MERS coronavirus-induced acute respiratory
303 distress syndrome. *Nat Microbiol* **2**, 16226, doi:10.1038/nmicrobiol.2016.226 (2016).

304 10 Bao, L. *et al.* The pathogenicity of SARS-CoV-2 in hACE2 transgenic mice. *Nature*,
305 doi:10.1038/s41586-020-2312-y (2020).

306 11 McCray, P. B., Jr. *et al.* Lethal infection of K18-hACE2 mice infected with severe acute
307 respiratory syndrome coronavirus. *J Virol* **81**, 813-821, doi:10.1128/JVI.02012-06
308 (2007).

309 12 Blanco-Melo, D. *et al.* Imbalanced Host Response to SARS-CoV-2 Drives Development
310 of COVID-19. *Cell* **181**, 1036-1045 e1039, doi:10.1016/j.cell.2020.04.026 (2020).

311 13 Rockx, B. *et al.* Comparative pathogenesis of COVID-19, MERS, and SARS in a
312 nonhuman primate model. *Science* **368**, 1012-1015, doi:10.1126/science.abb7314 (2020).

313 14 Gralinski, L. E. *et al.* Complement Activation Contributes to Severe Acute Respiratory
314 Syndrome Coronavirus Pathogenesis. *mBio* **9**, doi:10.1128/mBio.01753-18 (2018).

315 15 Dinnon, K. H., 3rd *et al.* A mouse-adapted model of SARS-CoV-2 to test COVID-19
316 countermeasures. *Nature*, doi:10.1038/s41586-020-2708-8 (2020).

317 16 Franks, T. J. *et al.* Resident cellular components of the human lung: current knowledge
318 and goals for research on cell phenotyping and function. *Proc Am Thorac Soc* **5**, 763-766,
319 doi:10.1513/pats.200803-025HR (2008).

320 17 Wahl, A. *et al.* Precision mouse models with expanded tropism for human pathogens. *Nat*
321 *Biotechnol* **37**, 1163-1173, doi:10.1038/s41587-019-0225-9 (2019).

322 18 Li, W. *et al.* Angiotensin-converting enzyme 2 is a functional receptor for the SARS
323 coronavirus. *Nature* **426**, 450-454, doi:10.1038/nature02145 (2003).

324 19 Raj, V. S. *et al.* Dipeptidyl peptidase 4 is a functional receptor for the emerging human
325 coronavirus-EMC. *Nature* **495**, 251-254, doi:10.1038/nature12005 (2013).

326 20 Hoffmann, M. *et al.* SARS-CoV-2 Cell Entry Depends on ACE2 and TMPRSS2 and Is
327 Blocked by a Clinically Proven Protease Inhibitor. *Cell* **181**, 271-280 e278,
328 doi:10.1016/j.cell.2020.02.052 (2020).

329 21 Walls, A. C. *et al.* Structure, Function, and Antigenicity of the SARS-CoV-2 Spike
330 Glycoprotein. *Cell* **181**, 281-292 e286, doi:10.1016/j.cell.2020.02.058 (2020).

331 22 Yan, R. *et al.* Structural basis for the recognition of SARS-CoV-2 by full-length human
332 ACE2. *Science* **367**, 1444-1448, doi:10.1126/science.abb2762 (2020).

333 23 Song, Z. *et al.* From SARS to MERS, Thrusting Coronaviruses into the Spotlight. *Viruses*
334 **11**, doi:10.3390/v11010059 (2019).

335 24 Meyerholz, D. K., Lambertz, A. M. & McCray, P. B., Jr. Dipeptidyl Peptidase 4
336 Distribution in the Human Respiratory Tract: Implications for the Middle East
337 Respiratory Syndrome. *Am J Pathol* **186**, 78-86, doi:10.1016/j.ajpath.2015.09.014
338 (2016).

339 25 Carsana, L. *et al.* Pulmonary post-mortem findings in a series of COVID-19 cases from
340 northern Italy: a two-centre descriptive study. *Lancet Infect Dis*, doi:10.1016/S1473-
341 3099(20)30434-5 (2020).

342 26 Menter, T. *et al.* Post-mortem examination of COVID19 patients reveals diffuse alveolar
343 damage with severe capillary congestion and variegated findings of lungs and other
344 organs suggesting vascular dysfunction. *Histopathology*, doi:10.1111/his.14134 (2020).

345 27 Tian, S. *et al.* Pulmonary Pathology of Early-Phase 2019 Novel Coronavirus (COVID-
346 19) Pneumonia in Two Patients With Lung Cancer. *J Thorac Oncol* **15**, 700-704,
347 doi:10.1016/j.jtho.2020.02.010 (2020).

348 28 Zhu, N. *et al.* A Novel Coronavirus from Patients with Pneumonia in China, 2019. *N*
349 *Engl J Med* **382**, 727-733, doi:10.1056/NEJMoa2001017 (2020).

350 29 Kim, D. *et al.* The Architecture of SARS-CoV-2 Transcriptome. *Cell* **181**, 914-921 e910,
351 doi:10.1016/j.cell.2020.04.011 (2020).

352 30 Xu, Z. *et al.* Pathological findings of COVID-19 associated with acute respiratory
353 distress syndrome. *Lancet Respir Med* **8**, 420-422, doi:10.1016/S2213-2600(20)30076-X
354 (2020).

355 31 Zhang, H. *et al.* Histopathologic Changes and SARS-CoV-2 Immunostaining in the Lung
356 of a Patient With COVID-19. *Ann Intern Med* **172**, 629-632, doi:10.7326/M20-0533
357 (2020).

358 32 Zhou, Z. *et al.* Heightened Innate Immune Responses in the Respiratory Tract of COVID-
359 19 Patients. *Cell Host Microbe* **27**, 883-890 e882, doi:10.1016/j.chom.2020.04.017
360 (2020).

361 33 Spiegel, M. *et al.* Inhibition of Beta interferon induction by severe acute respiratory
362 syndrome coronavirus suggests a two-step model for activation of interferon regulatory
363 factor 3. *J Virol* **79**, 2079-2086, doi:10.1128/JVI.79.4.2079-2086.2005 (2005).

364 34 Siu, K. L. *et al.* Severe acute respiratory syndrome coronavirus M protein inhibits type I
365 interferon production by impeding the formation of TRAF3.TANK.TBK1/IKKepsilon
366 complex. *J Biol Chem* **284**, 16202-16209, doi:10.1074/jbc.M109.008227 (2009).

367 35 Qin, C. *et al.* Dysregulation of immune response in patients with COVID-19 in Wuhan,
368 China. *Clin Infect Dis*, doi:10.1093/cid/ciaa248 (2020).

369 36 Hou, Y. J. *et al.* SARS-CoV-2 Reverse Genetics Reveals a Variable Infection Gradient in
370 the Respiratory Tract. *Cell*, doi:10.1016/j.cell.2020.05.042 (2020).

371

372

373

374

375

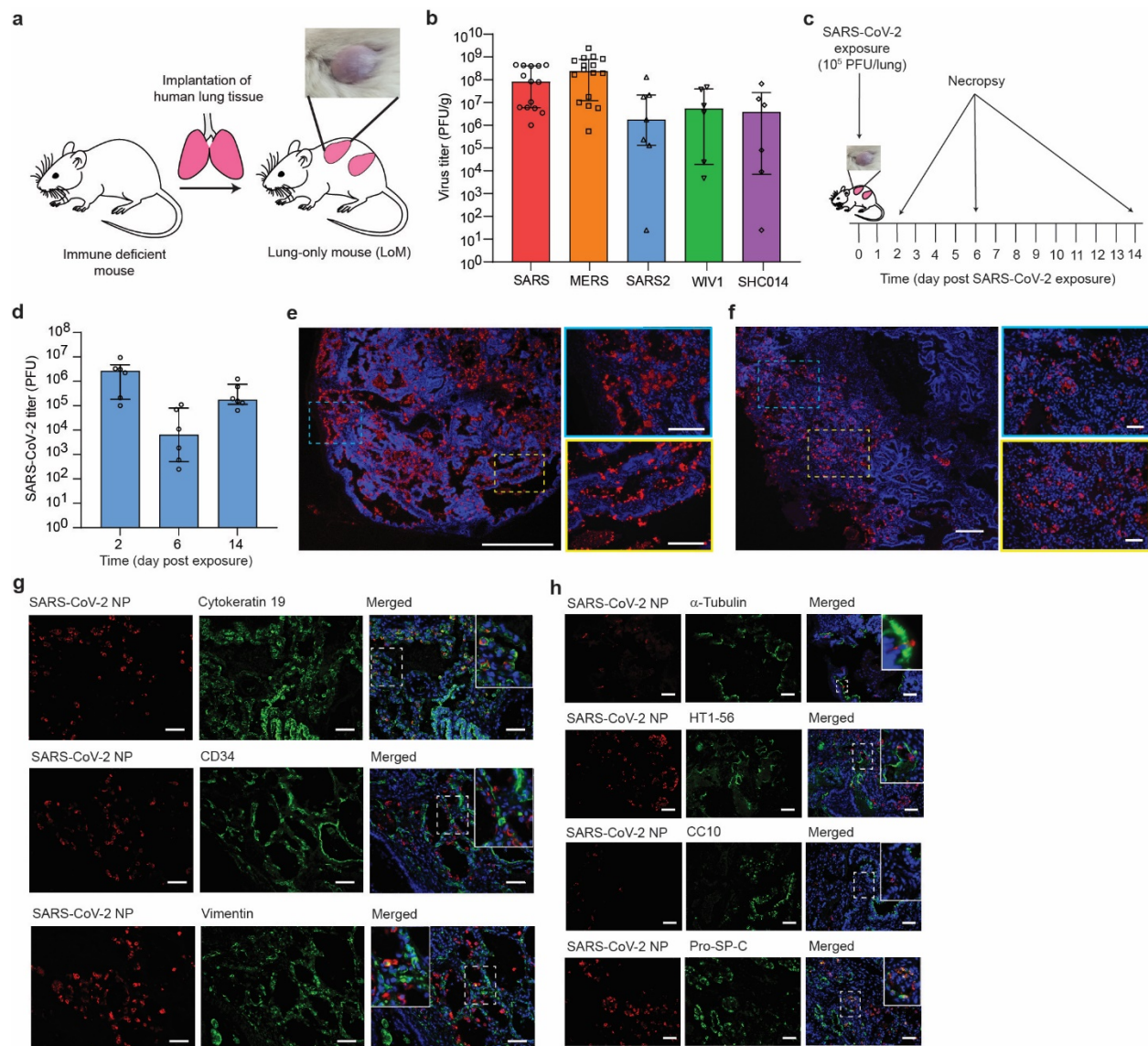


Fig. 1. Robust replication of recently emerged human and bat coronaviruses in LoM demonstrate the potential of bat coronaviruses for direct transmission to humans and the predilection of SARS-CoV-2 for infection of human epithelial cells.

a, Construction of LoM and image of a human lung implant. **b**, Titers of virus in the human lung tissue of LoM directly injected with SARS-CoV (n=14, red), MERS-CoV (n=16, orange), SARS-CoV-2 (n=7, blue), WIV1-CoV (n=6, green), or SHC014 (n=6, purple) as determined by plaque assay (PFU, plaque forming units). **c**, SARS-CoV-2 was directly injected into the human lung tissue of LoM. Human lungs were collected at days 2, 6, and 14 post-infection. **d**, SARS-CoV-2 titers in the human lung tissue of LoM

at days 2 (n=6), 6 (n=6), and 14 (n=6) post-exposure. **e**, In situ hybridization RNAscope for SARS-CoV-2 RNA in LoM human lung tissue 2 days post-exposure (SARS-CoV-2 RNA+, red; nuclei, blue; scale bars, 750 um [left image] and 250 um [right image]). **f**, Immunofluorescence staining for virus nucleoprotein in LoM human lung tissue two-days post-exposure (positive cells, red; nuclei, blue; scale bars 200 um [top image] and 50 um [bottom images], n=6 analyzed). **g**, Co-staining of LoM human lung tissue two days following SARS-CoV-2 exposure for virus nucleoprotein (red) and cytokeratin 19 (epithelial cells, green, n=6 analyzed), CD34 (endothelial cells, green, n= 4 analyzed), or vimentin (mesenchymal cells, green, n=4 analyzed). Nuclei, blue; scale bars 50 um. **h**, Co-staining of LoM human lung tissue two days following SARS-CoV-2 exposure for virus nucleoprotein (red) and acetylated alpha-tubulin IV (ciliated cells, green, n=6 analyzed), CC10 (club cells, green, n=6 analyzed), HT1-56 (alveolar type 1 cells, green, n=6 analyzed), or Pro-SP-C (alveolar type 2 cells, green, n=3 analyzed). Nuclei, blue; scale bars 50 um. In **b** and **c**, horizontal and vertical lines represent the median and interquartile range respectively.

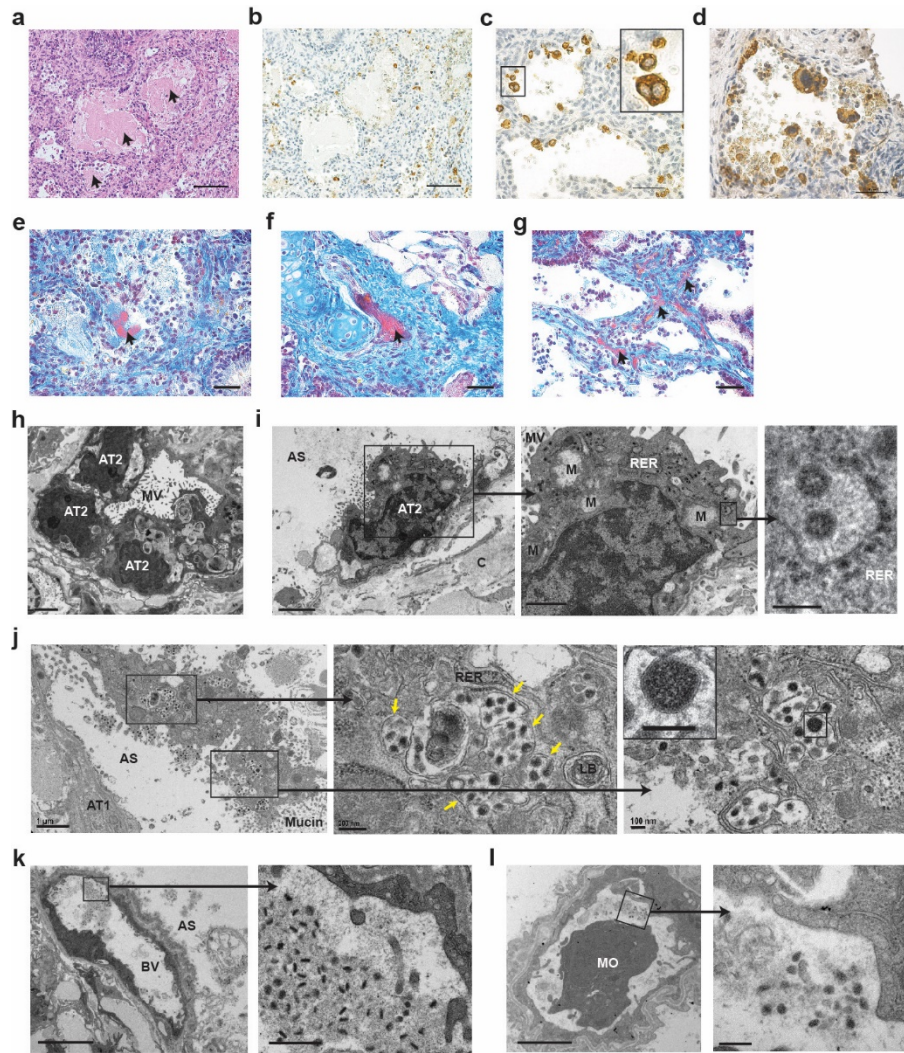


Fig. 2. During acute infection, SARS-CoV-2 is highly cytopathic and causes extensive damage to human lung structures.

a, H&E staining of a SARS-CoV-2 infected LoM human lung tissue 2 days post-exposure (scale bar, 100 um, n=6 analyzed). Globules of protein material are indicated with arrows. **b-d**, Immunohistochemical staining for virus nucleoprotein in LoM human lung tissue 2 days following SARS-CoV-2 exposure (positive cells, brown; **b** scale bars, 100 um; **c** and **d** scale bars, 50 um, n=6 analyzed). **e-g**, Martius Scarlet Blue staining of a SARS-CoV-2 infected LoM human lung tissue 2 days post-exposure (scale bars, 50 um; fibrin, red; collagen, blue, n=6 analyzed). Arrows indicate the presence of fibrin (red) in **e**, alveoli or in **f** and **g**, thrombi of occluded vessels. **h-l**, Electron microscopy analysis of SARS-CoV-2

infected human lung tissue two days post-exposure (n=3 analyzed). **h**, Uninfected AT2 cells in an alveolus-like structure. Scale bars, 2 μ m. **i**, SARS-CoV-2 infected AT2 cell. Higher magnification images of areas indicated with black boxes show virus particles with dense nucleocapsids in RER. Scale bars, 2 μ m (left image), 1 μ m (middle image), and 200 nm (right image). **j**, A degenerative SARS-CoV-2 infected cell in the alveolar space. Vesicles filled with virus particles in the middle image are indicated with arrows. Scale bars, 1 μ m (left image), 200 nm (middle image), and 100 nm (right image). **k** and **l**, Blood vessels containing virions, fibrillar protein and cell debris. In **k**, scale bars, 5 μ m (left image) and 500 nm (right image). In **l**, scale bars, 2 μ m (right image) and 200 nm (left image). AS, alveolar space; AT1, alveolar type 1 cells; AT2, alveolar type 2 cells; BV, blood vessel; C, collagen; LB, lamellar body; M, mitochondria; MO, monocyte; MV, microvilli; RER, rough endoplasmic reticulum. In **c**, **i-l**, black boxes indicate areas of higher magnification images.

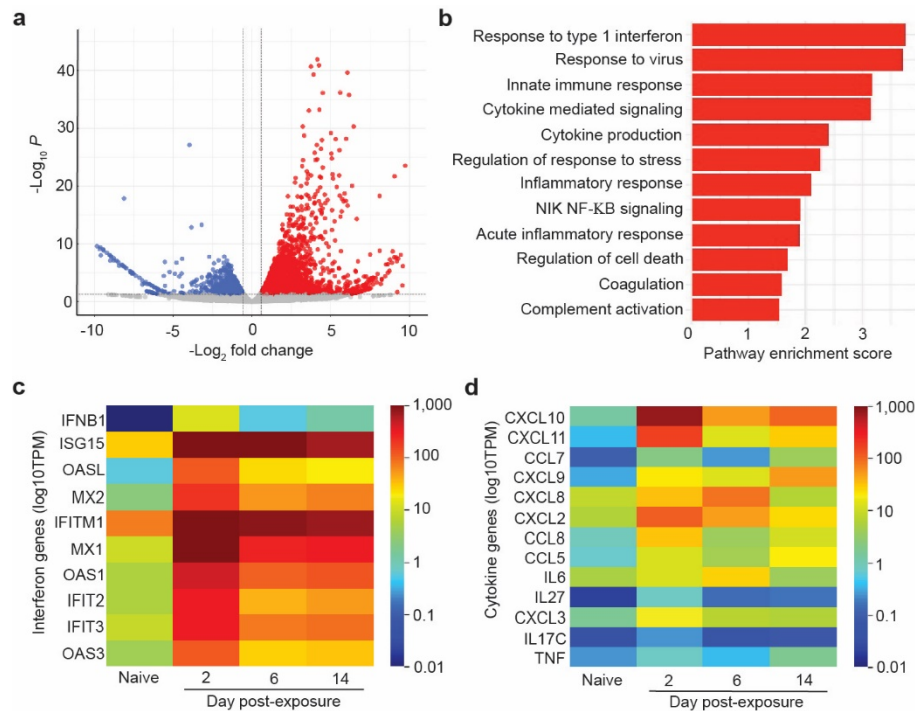


Fig. 3. SARS-CoV-2 infection induces a strong and sustained host innate immune response in human lung tissue.

a-d, RNA-sequencing analysis of human lung tissue collected from SARS-CoV-2 infected LoM. **a**, The plot depicts the up-regulated (red) and down-regulated (blue) genes in SARS-CoV-2 infected human lung tissue two days post-infection (n=2) compared to human lung tissue from naïve LoM (n=2). The mean $-\log_2$ -transformed fold change and the multiple testing adjusted $-\log_{10}$ p value are shown on the x-axis and y-axis respectively. Dashed lines show the thresholds of \log_2 -transformed fold change of 1.5 and adjusted $p < 0.05$. **b**, Gene set enrichment analysis (GSEA) identified gene sets enriched in SARS-CoV-2 infected LoM human lungs (red, $p < 0.05$). The pathway enrichment score is shown on the x-axis. Heatmaps illustrating the expression of human **c**, interferon genes and **d**, cytokine/chemokine genes in human lung tissue collected analyzed from SARS-CoV-2 infected LoM days 2 (n=2), 6 (n=3), and 14 (n=3) post-exposure and naïve LoMs (n=4). Color scale indicates the mean \log_{10} transcripts per million (TPM).

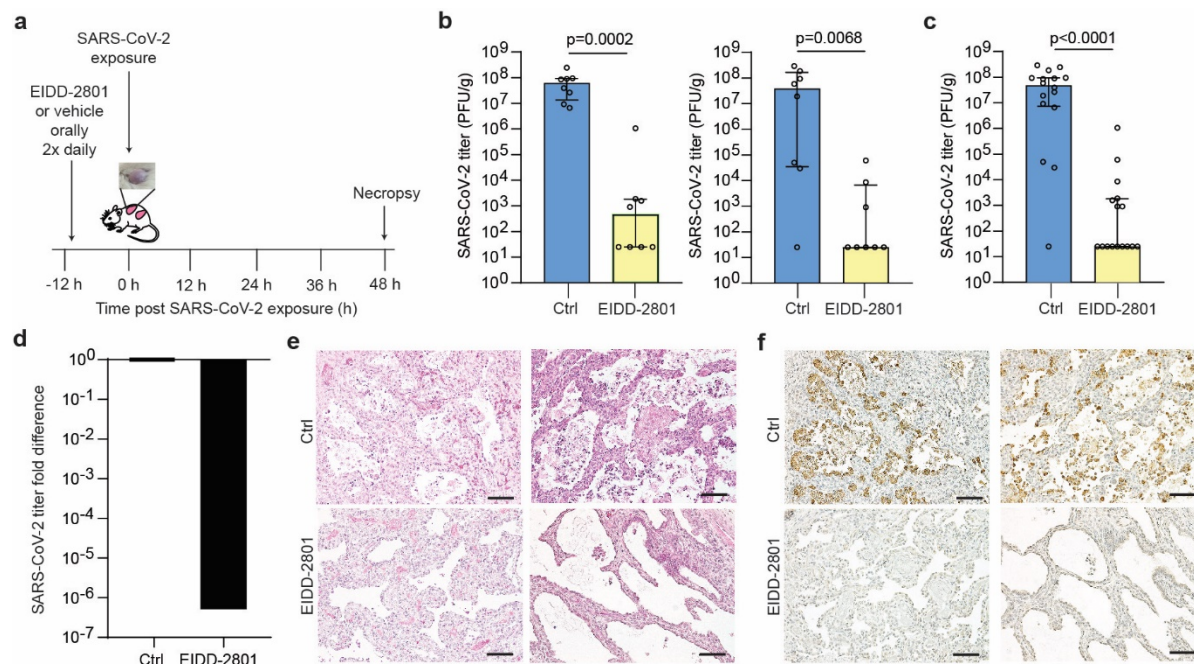


Fig. 4. Pre-exposure prophylaxis with EIDD-2801, a broad-spectrum anti-coronavirus drug, potently prevents SARS-CoV-2 infection *in vivo*.

a, Experimental design. LoM were administered EIDD-2801 or vehicle control 12 h prior to SARS-CoV-2 exposure and every 12 h thereafter. Virus titers in human lung tissues were measured 2 days post-exposure. **b** and **c**, SARS-CoV-2 titers in the human lung tissue of LoM administered EIDD-2801 ($n=8$ per experiment, yellow) or control vehicle (Ctrl, $n=8$ per experiment, blue) at 2 days post-exposure in two independent experiments shown **b**, separately and **c**, combined. Titers were compared with a two-tailed Mann-Whitney U test. Horizontal and vertical lines represent the median and interquartile range respectively. **d**, Fold difference in SARS-CoV-2 titers in the human lung tissue of LoM relative to vehicle controls. **e**, H&E staining and **f**, immunohistochemical staining for virus nucleoprotein (positive cells, brown) of human lung tissue of LoM administered EIDD-2801 ($n=8$ analyzed) or control vehicle (Ctrl, $n=8$ analyzed) at 2 days post-exposure (scale bars, 100 μ m).

Methods

Experimental design

Human lung-only mice (LoM) were used as an *in vivo* model to evaluate infection of lung tissue with recombinant coronaviruses SARS-CoV, MERS-CoV, and SARS-CoV-2 as well as full length bat coronaviruses WIV1 and SHC014^{4,5,37,38}. Viruses were directly injected into the human lung tissue of LoMs and lung tissue collected either 2, 6, or 14 days post-exposure for virus titer determination and/or analysis by histology, electron microscopy, or RNA-seq.

Construction of humanized mice

LoMs were constructed with 1-2 human lung implants by surgically implanting human lung tissue (Advanced Bioscience Resources) subcutaneously into the upper and lower back of male and female 12-21 week old NOD.Cg-Prkdc^{scid} Il2rg^{tm1Wjl}/SzJ mice [NSG mice; The Jackson Laboratory] as previously described¹⁷. Engraftment of lung tissue was assessed by palpation and by 8 weeks post-surgery animals were ready for experimentation. Mice were housed and maintained by the Division of Comparative Medicine at the University of North Carolina-Chapel Hill and in accordance to the NIH Guide for the Care and Use of Laboratory Animals.

Production of coronavirus stocks and infection of humanized mice

Stocks of wild-type SARS-CoV, MERS-CoV (HCoV-EMC/2012), SHC014-CoV, and WIV1-CoV were derived from infectious virus clones and were prepared and titered on Vero E6 (SARS-CoV, SHC014-CoV, and WIV1-CoV) or Vero CCL81 cells (MERS-CoV) (American Type Culture Collection) as previously described^{4,5,9,17}. A clinical isolate of SARS-CoV-2 (2019-nCoV/USA-WA1/2020) was obtained from the U.S. Centers for Disease Control and Prevention

(GenBank accession no. MN985325.1) and passaged twice in Vero E6 cells to create a passage 5 working stock³⁶. For the infection of mice with coronavirus, the fur over the human lung tissue of anesthetized mice was shaved and virus (10^5 PFU in 100 μ l PBS or 3×10^5 PFU in 100 μ l PBS for bat coronavirus inoculations) was injected directly into the lung tissue. To evaluate the *in vivo* inhibitory activity of EIDD-2801, mice were administered 500 mg/kg EIDD-2801 or vehicle control (10% PEG and 2.5% Cremophor RH40 in water) via oral gavage starting 12 h prior to SARS-CoV-2 exposure and every 12 h thereafter. At necropsy, human lung tissues were collected, weighed, homogenized, and stored at -80°C until titrating on Vero E6 cells. Titers below the limit of the assay (50 PFU/mL) were assigned a value of 25 PFU/gram.

H&E staining of human lung tissue

Human lung tissues collected from LoM were fixed in 10% formalin, paraffin embedded, and cut into 5 μ m sections which were mounted onto Superfrost Plus slides (Fisher Scientific). Tissue sections were incubated at 60°C for 1 h, deparaffinized with xylene (2×3 min) and graded ethanol (100% 2×3 min, 95% 1×3 min, 80% 1×3 min, 70% 1×3 min), and stained with hematoxylin followed by eosin. Tissue sections were then mounted and imaged on a Nikon Eclipse Ci microscope using Nikon Elements BR software (version 4.30.01) with a Nikon Digital Sight DS-Fi2 camera. Brightness, contrast and white balance were adjusted on whole images in Adobe Photoshop (CS6).

Immunohistochemical analysis of coronavirus infection

Immunohistochemistry was performed as previously described¹⁷. Briefly, fixed (10% formalin) human lung tissues collected from coronavirus-infected LoM were paraffin embedded and

sectioned (5 μ m). Tissue sections mounted on Superfrost Plus slides (Fisher Scientific) were deparaffinized as described above. Following antigen retrieval using Diva Decloaker (BioCare Medical), non-specific binding was blocked using Background Sniper (BioCare Medical). Tissue sections were then incubated with primary antibodies against SARS-CoV or MERS-CoV nucleocapsid overnight at 4°C. Tissue sections incubated with rabbit IgG were used as isotype controls. Tissue sections were then washed in TBST and the endogenous peroxidase activity blocked with hydrogen peroxide. Tissue sections were developed using the MACH-3 polymer system (BioCare Medical) and 3,3'-diaminobenzidine (DAB) (Vector Laboratories), counterstained with hematoxylin, and mounted. Tissue sections were imaged on a Nikon Eclipse Ci microscope using Nikon Elements BR software (version 4.30.01) with a Nikon Digital Sight DS-Fi2 camera. Adobe Photoshop (CS6) was used to adjust brightness, contrast and white balance on whole images.

Immunofluorescence analysis of SARS-CoV2 infection

Human lung tissues collected from mice were fixed in 10% formalin and paraffin embedded. Immunofluorescence staining of 5 μ m tissue sections was performed as previously described¹⁷. Briefly, following deparaffinization and antigen retrieval (Diva Decloaker), tissue sections were incubated with a 10% normal donkey serum solution with 0.1% Triton X-100 in 1x PBS to block non-specific binding. Tissue sections were then incubated overnight with primary antibodies at 4°C followed by incubation with fluorescent conjugated secondary antibodies (Supplementary Table 7). Primary antibodies were directed against SARS nucleoprotein and human cytokeratin 19, CD34, vimentin, acetylated alpha-tubulin IV, CC10, HT1-56, and pro-SP-C (Supplementary Table 7). Background autofluorescence was then quenched using a 0.1% Sudan Black B

solution in 80% ethanol prior to staining with DAPI. Slides were mounted and then imaged using an Olympus BX61 upright wide-field microscope using Volocity software (version 6.3) with a Hamamatsu ORCA RC camera. Appropriate negative controls without primary antibodies were also imaged using the same exposure time as matching stained sections. Whole image contrast, brightness, and pseudocoloring were adjusted using ImageJ/Fiji (Version 2.0.0-rc-69/1.51w) and Adobe Photoshop (version CS6).

RNA in situ hybridization (RNA-ISH) analysis of SARS-CoV2 infection

RNA-ISH was performed on 10% formalin fixed, paraffin-embedded, 5 µm sections of human lung tissues using the RNAscope 2.5 HD Reagent Kit according to the manufacturer's instructions (Advanced Cell Diagnostics). Briefly, tissue sections were mounted on Superfrost Plus microscope slides (Fisher Scientific), heated at 60°C for 1 h, deparaffinized in xylene (2 x 5 minutes) and 100% ethanol (2x2 minutes), and air-dried. Tissue sections were then incubated with hydrogen peroxide to block endogenous peroxidases for 10 min at RT, followed by epitope retrieval (Advanced Cell Diagnostics) for 30 min in a 95°C water bath. Subsequently, tissue sections were immediately washed in double distilled water then dehydrated in 100% ethanol for 2 min before air-drying. Tissue sections were then incubated with Protease Plus (Advanced Cell Diagnostics) for 30 min at 40°C in a HybEZ hybridization oven (Advanced Cell Diagnostics). Sections were rinsed 3 times in double distilled water and then incubated with pre-warmed target probe designed to hybridize with the spike protein of SARS-CoV-2 (Cat. Number 848561, Advanced Cell Diagnostics) for 2 h at 40°C. Tissue sections were then washed and the signal amplified according to the manufacturer's instructions and developed using alkaline phosphatase

and Fast Red substrate. Tissue sections were counterstained with DAPI, mounted with Prolong® Gold (Invitrogen), and imaged on an EVOS M5000 microscope (Invitrogen).

Electron microscopy analysis of SARS-CoV2 infection

Small pieces of human lung tissue collected from SARS-CoV-2 infected LoM at two days post-infection were fixed in 4% paraformaldehyde/2.5% glutaraldehyde in 0.15 M sodium phosphate buffer, pH 7.4, for 2 h at RT. The tissues were subsequently transferred to 10% formalin for 7 days. Specimens were washed in 0.1 M sodium cacodylate, pH 7.4, then post-fixed with 1% cacodylate-buffered osmium tetroxide for 1 h. After washing in 0.05 M sodium cacodylate buffer, pH 7.0, the samples were treated with 1% tannic acid in 0.05 M sodium cacodylate buffer for 30 min to enhance tissue contrast and preserve structure³⁹. Tissue pieces were washed in deionized water, dehydrated in ethanol, and placed through two exchanges of propylene oxide before infiltration and embedment in PolyBed 812 epoxy resin (Polysciences). Semi-thin (1 µm) sections of tissue blocks were cut and stained with 1% toluidine blue in 1% sodium borate for examination by light microscopy. Ultra-thin (70 nm) sections were cut of selected regions of interest, mounted on 200 mesh copper grids and stained with 4% aqueous uranyl acetate and Reynolds' lead citrate. Grids were observed on a JEOL JEM 1230 transmission electron microscope operating at 80kV (JEOL USA, Inc.) and images were acquired with a Gatan Orius SC1000 CCD Digital Camera and Gatan Microscopy Suite software (version 3.0, Gatan, Inc.). Virus particle sizes were measured in Fiji/Image J (version 2.0.0-rc-69/1.52p).

Processing of human lung tissues for RNA-sequencing analysis

Human lung tissues were collected in RNAlater and kept at 4°C for 24 h prior to storage at -80°C until further processing. To isolate RNA, samples stored in RNAlater were thawed and the tissue transferred to a new tube containing 1 mm glass beads and 1 mL Trizol. Tissues were subsequently homogenized using a MagNA Lyser (Roche) for 30 sec at 6,000 rpm. In between rounds of homogenization, tissues were incubated on ice for 1 min. Following tissue homogenization, Trizol homogenate was transferred to a new tube and stored at -80°C.

RNA-sequencing analysis

RNA was extracted from lung samples using a Trizol Plus RNA extraction kit (Thermo Fisher), quantified using a Qubit RNA assay kit and checked for quality using a Bioanalyzer RNA600 Nano kit (Agilent). RNA integrity scores were typically 7.0 and greater. 1ug of RNA was used to construct libraries for sequencing using a NEBNext Ultra II library prep kit with polyA RNA selection. Barcoded libraries were sequenced on a Novaseq 6,000 2x100 bp following manufacturer's instructions (Illumina). Sequence quality was assessed using FASTQC (v). No issues were detected with the data and quality was typical for RNA extracted from fresh frozen material. A small amount of index hopping was detected (0.09%) due to the single indices used in the library preparation. Raw reads were mapped to the human, mouse, and SARS-CoV-2 reference genomes simultaneously (GRCh38.p13, GRCm38.p6 M25, NC_045512, respectively) using the BBSplit function in BBmap (version 38.86). This step minimized cross mapping of reads among genomes. We then mapped and quantified on a transcript and gene model basis using STAR (version 2.7.5a) and Salmon (version 1.2.1)^{40,41}. Reads mapping to multiple locations were dropped from analysis. On average, in the lung tissue samples from LoM mice, 80% of the reads mapped to human (standard deviation: +/- 6%), 19% mapped to mouse

(standard deviation: +/- 6%) and 1% mapped to the SARS-Cov-2 genome (standard deviation: +/- 1%). The percent of virus ranged from 0.05% to 3.4% among infected mice, with day 2 mice having the most, which is consistent with the infection titers observed. Samples from naïve mice were 95% or more human data.

Statistical analysis

RNA-sequencing data was normalized and interrogated for changes in gene expression using DESeq2 package (version 3.1.1) in R (version 3.6.3)⁴². We focused the analysis on the naïve controls versus LoM for days 2, 6, and 14 post-infection. Wald's tests were performed contrasting each day versus naïve controls. Because mice were sacrificed at each time point, we treated each day independently and not as a time series. *P*-values were adjusted for multiple testing using a False Discovery Rate using the Benjamini & Hochberg method⁴³. Data was analyzed both jointly and within each treatment compared to naïve controls. Differential expression of outliers was assessed and found insignificant in overall effect. Graphs and summary tables were built in R using ggplot; gene set enrichment was performed using GSEA and GO analysis (tidyverse 1.3.0; PCATools 1.2.0; Sqldf 0.4-11; na.tools 0.3.1; ggbiplot 0.55; ggplot2 3.3.1; dplyr 0.8.4). Specific gene sets of interest were then interrogated for patterns of expression across treatment and time using unsupervised clustering of normalized gene expression counts. Gene Ontology (GO) analysis and visualization were performed with GOrilla⁴⁴. Data was uploaded to the NCBI GEO archive (accession: GSE155286). Virus titers between vehicle control and EIDD-2801 treated LoM were compared with a two-tailed Mann-Whitney U test.

Methods References

- 37 Scobey, T. *et al.* Reverse genetics with a full-length infectious cDNA of the Middle East respiratory syndrome coronavirus. *Proc Natl Acad Sci U S A* **110**, 16157-16162, doi:10.1073/pnas.1311542110 (2013).
- 38 Yount, B. *et al.* Reverse genetics with a full-length infectious cDNA of severe acute respiratory syndrome coronavirus. *Proc Natl Acad Sci U S A* **100**, 12995-13000, doi:10.1073/pnas.1735582100 (2003).
- 39 Simionescu, N. & Simionescu, M. Galloylglucoses of low molecular weight as mordant in electron microscopy. I. Procedure, and evidence for mordanting effect. *J Cell Biol* **70**, 608-621, doi:10.1083/jcb.70.3.608 (1976).
- 40 Dobin, A. *et al.* STAR: ultrafast universal RNA-seq aligner. *Bioinformatics* **29**, 15-21, doi:10.1093/bioinformatics/bts635 (2013).
- 41 Patro, R., Duggal, G., Love, M. I., Irizarry, R. A. & Kingsford, C. Salmon provides fast and bias-aware quantification of transcript expression. *Nat Methods* **14**, 417-419, doi:10.1038/nmeth.4197 (2017).
- 42 Love, M. I., Huber, W. & Anders, S. Moderated estimation of fold change and dispersion for RNA-seq data with DESeq2. *Genome Biol* **15**, 550, doi:10.1186/s13059-014-0550-8 (2014).
- 43 Benjamini, Y. & Hochberg, Y. Controlling the False Discovery Rate: A Practical and Powerful Approach to Multiple Testing. **57**, 289-300, doi:10.1111/j.2517-6161.1995.tb02031.x (1995).

44 Eden, E., Navon, R., Steinfeld, I., Lipson, D. & Yakhini, Z. GOrilla: a tool for discovery
and visualization of enriched GO terms in ranked gene lists. *BMC Bioinformatics* **10**, 48,
doi:10.1186/1471-2105-10-48 (2009).

Acknowledgements: We thank current and past members of the Garcia laboratory for technical
assistance. The authors also thank technicians at the UNC Animal Histopathology and
Laboratory Animal Medicine Core and Division of Comparative Medicine. We also thank the
UNC School of Medicine Bioinformatics and Analytics Research Collaborative (BARC) for
providing technical support and K. Mollan and B. Shook-Sa of the UNC CFAR Biostatistics
Core for providing statistical support. **Funding:** This work was supported by funding from
National Institutes of Health grants R21AI113736 (RJP), U19AI100625 (RSB), R21AI145372
(LEG), R01AI123010 (AW), R01AI111899 (JVG), R01AI140799 (JVG), R01MH108179
(JVG). The Microscopy Services Laboratory, Department of Pathology and Laboratory
Medicine, is supported in part by P30 CA016086 Cancer Center Support Grant to the UNC
Lineberger Comprehensive Cancer Center.

Author contributions: AW, CEJ, WY, MK, and CD constructed LoM. AW contributed to
experimental design, data interpretation, data presentation, and manuscript writing, coordinated
the study, and the preparation of the manuscript. LEG performed the virus inoculations, animal
necropsies, virus titrating, processing of lung tissues for RNA extraction, and contributed to the
experimental design, planning, data analysis, data interpretation, and manuscript writing. CEJ
performed immunofluorescence and H&E analyses, WY performed immunohistochemistry and
H&E analyses, and MK performed the in-situ hybridization analysis of LoM human lung tissues.

KHD, AS, SRL, and KG assisted with the *in vivo* experiments with coronavirus-infected LoMs. VJM in conjunction with KKW performed the electron microscopy analysis. FBA assisted with the pathohistological analysis. HL, HMK, TZ, POG, performed the RNA-sequencing analysis. EPB and CDJ contributed to design of RNA-sequencing experiments. RJP assisted with the immunofluorescence analysis and contributed to experimental design, data interpretation, data presentation, and manuscript writing. RSB conceived and designed experiments and contributed to data interpretation and manuscript writing. JVG conceived, designed and coordinated the study, conceived and designed experiments, and contributed to data interpretation, data presentation, and manuscript preparation.

Competing interests: The authors have no competing interests.

Additional Information

Supplementary information is available for this paper at

Correspondence: Correspondence to J. Victor Garcia.

Reporting summary

Further information on research design is available in the Nature Research Reporting Summary linked to this paper.

697 **Data availability:** Gene-expression data are available at the Gene Expression Omnibus (GEO)
698 repository (accession: GSE155286). All other data is available in the manuscript or the
699 supplementary materials.

700

701

702

703

704

705

706

707

708

709

710

711

712

713

714

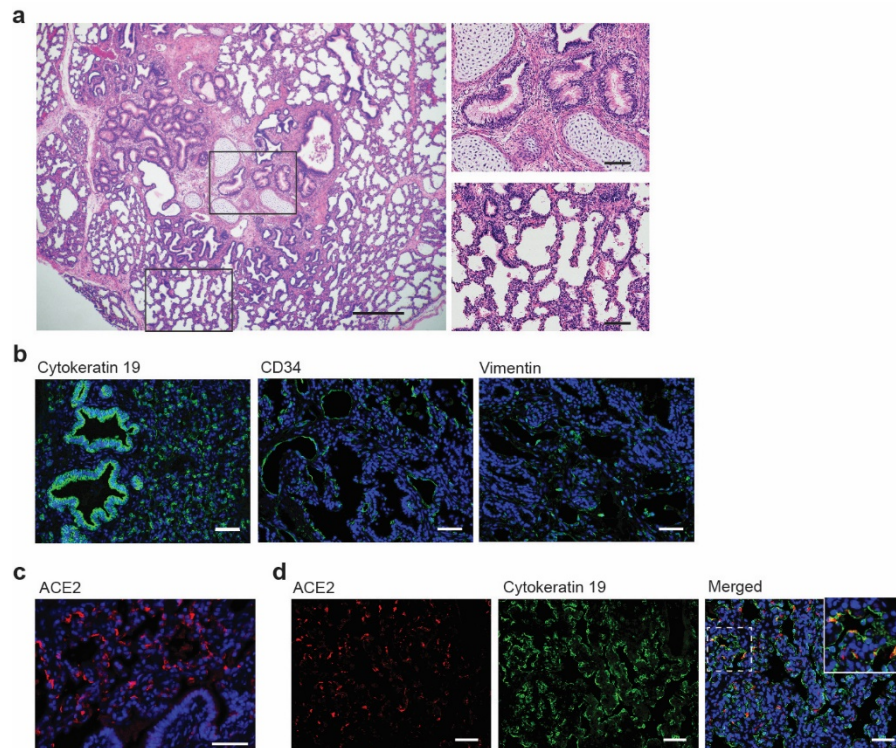
715

716

717

718

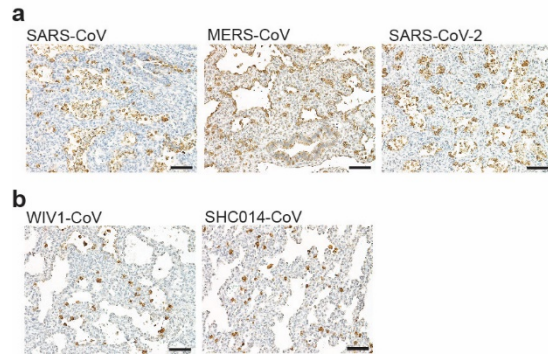
719



Extended Data Fig. 1. Human epithelial cells in the human lung tissue of LoMs express

ACE2.

a, H&E staining of the human lung tissue of a naïve LoM (scale bars 500 μm [left image] and 100 μm [right images], n=6 analyzed). Boxes indicate regions shown in higher magnification images (right images) of cartilaginous airways (top) and non-cartilaginous airways and alveoli (bottom). Immunofluorescence staining for **b**, human cytokeratin 19 (epithelial cells, green; nuclei, blue; scale bar 50 μm), CD34 (endothelial cells, green; nuclei, blue; scale bar 50 μm), and vimentin (mesenchymal cells, green; nuclei, blue; scale bar 50 μm). n=8 analyzed. **c**, human ACE2 in the human lung tissue of a naïve LoM (positive cells, red; nuclei, blue; scale bar 50 μm, n=9 analyzed). **d**, Co-staining for human ACE2 (positive cells, red) and cytokeratin 19 (positive cells, green) in naïve LoM human lung tissue (nuclei, blue; scale bar 50 μm, n=9 analyzed).



Extended Data Fig. 2. Viral nucleoprotein in the human lung tissues of LoM infected with recently emerged human coronaviruses and bat coronaviruses.

Immunohistochemical staining for virus nucleoprotein in human lung tissue collected from LoM two days post exposure to 10^5 PFU **a**, recently emerged human coronaviruses SARS-CoV (n=4 analyzed), MERS-CoV (n=5 analyzed), or SARS-CoV-2 (n=6 analyzed), or to **b**, bat coronaviruses WIV1-CoV or SHC014-CoV (positive cells, brown; scale bars, 100 μm, n=10 analyzed).

Group	Mouse	Sex	Human Donor	Weeks Post-Surgery
SARS-CoV	1	F	O32	10
	2	F	O32	10
	3	M	U32	9
	4	M	U32	9
	5	F	I33	14
	6	F	L33	10
	7	F	L33	10
	8	F	L33	10
MERS-CoV	9	M	D33	9
	10	M	D33	9
	11	M	F33	9
	12	M	F33	9
	13	F	I33	14
	14	F	L33	10
	15	F	L33	10
	16	F	L33	10
SARS-CoV-2	17	F	O32	19
	18	F	O32	19
	19	M	D33	14
	20	M	F33	14
WIV-CoV	21	M	F33	20
	22	M	F33	20
	23	M	F33	20
SHC014-CoV	24	M	F33	20
	25	M	F33	20
	26	M	F33	20

Extended Data Table 1. Description of LoM used for the analysis of human and bat coronavirus replication.

793

Group	Mouse	Sex	Human Donor	Weeks Post-Surgery
Day 2	27	F	A31	59
	28	F	A31	59
	29	F	F32	25
	30	F	I32	19
Day 6	31	F	R30	74
	32	F	A31	59
	33	F	I32	19
	34	F	F32	25
	35	F	F32	25
Day 14	36	F	A31	59
	37	F	I32	19
	38	F	R30	74
	39	F	F32	25
	40	F	F32	25

794 **Extended Data Table 2. Description of LoM used for the analysis of SARS-CoV-2**

795 **replication and pathogenesis over time.**

796
797
798
799
800
801
802
803
804
805
806
807
808
809
810
811
812
813
814
815
816
817
818
819
820
821
822
823
824
825
826

Group	Mouse	Sex	Human Donor	Weeks Post-Surgery	%Viral Transcripts
Day 2	1	F	A31	59	0.55301%
	41	F	I32	19	3.55979%
Day 6	31	F	R30	74	1.01818%
	32	F	A31	59	0.46368%
	33	F	I32	19	1.38159%
Day 14	37	F	I32	19	0.69389%
	39	F	F32	25	0.05856%
	42	F	A31	59	0.18557%
Naive	43	F	A31	59	N/A
	44	F	I32	19	N/A
	45	F	I32	19	N/A
	46	F	I32	19	N/A

Extended Data Table 3. Abundance of viral transcripts detected in SARS-CoV-2 infected

LoM.

Shown is the %viral transcripts of total transcripts sequenced from SARS-CoV-2 infected LoM utilized for RNA-sequencing analysis. Not applicable: N/A

	Gene	Naive	Day 2		Day 6			Day 14			
		TPM	TPM	Log2FC	p-value	TPM	Log2FC	p-value	TPM	Log2FC	p-value
Interferon genes	IFNB1	0.009721	12.89298	10.8264	5.35E-15	0.56133	5.919101	0.000104	1.261203	6.816893	8.95E-07
	ISG15	29.11072	3529.547	7.5504869	7.47E-104	1057.532	5.559945	N/A	680.674	4.441103	4.38E-18
	OASL	0.575651	117.7447	7.460388	2.09E-49	24.14577	5.349643	4.82E-21	19.32386	4.837053	3.70E-40
	MX2	2.446529	207.3412	7.1723067	4.92E-50	54.58907	4.403233	4.35E-16	73.59163	4.793127	3.89E-23
	IFITM1	75.8737	1380.718	6.8014838	8.56E-107	841.8657	3.67271	0.027036	752.1089	3.183608	0.056391
	MX1	10.01414	1098.343	6.6205208	1.61E-48	282.2782	4.583841	1.03E-35	320.7999	4.690323	9.58E-119
	OAS1	5.455972	427.8919	6.3944922	1.69E-48	109.1991	4.097581	4.61E-13	128.1803	4.407948	4.03E-33
	IFIT2	5.663018	327.3042	5.8248817	1.46E-15	40.06805	2.678602	1.04E-12	51.76333	3.021741	3.65E-11
	IFIT3	9.293879	323.3581	5.5590143	5.29E-24	77.21678	2.973115	3.24E-09	90.51719	3.168749	9.62E-11
OAS3	4.160792	118.0739	5.1575147	2.43E-19	27.98228	2.619502	5.04E-13	32.44652	3.006743	1.07E-25	
Cytokine genes	CXCL10	1.334587	784.985	9.4483016	7.54E-07	51.89486	5.060381	3.36E-08	104.6776	6.211797	2.26E-28
	CXCL11	0.368657	170.7106	9.0255049	1.90E-06	13.74948	5.100041	1.73E-13	28.97534	6.20993	4.12E-32
	CCL7	0.110614	2.114279	8.1032148	1.56E-07	0.256785	0.939467	0.826964	4.136358	5.155454	0.0337375
	CXCL9	0.31541	20.86055	6.5863786	0.0085582	13.58781	5.142114	N/A	51.63909	7.324334	N/A
	CXCL8	8.329686	33.28712	6.3670255	4.21E-18	88.08344	2.850492	N/A	6.213093	-0.60592	N/A
	CXCL2	6.093913	114.8106	5.9559545	1.13E-15	51.26291	2.979872	0.018944	24.8723	2.026886	0.1230292
	CCL8	0.872448	31.60003	5.7008898	6.14E-14	3.819344	2.129537	0.000334	11.39742	3.657159	2.66E-05
	CCL5	0.708453	12.48674	5.5750578	1.74E-16	4.494502	2.620838	0.029157	19.43851	4.710446	7.17E-05
	IL6	5.42304	12.23683	5.0378314	0.01548861	27.2112	1.542807	N/A	3.889728	-0.96496	N/A
	IL27	0.02044	0.802539	4.5555662	0.00022349	0.144501	2.957134	0.168998	0.166259	2.840334	0.0473019
	CXCL3	1.665821	17.51558	4.0723405	6.74E-13	7.100009	2.13156	0.03234	6.128888	1.776734	0.0077687
	IL17C	0.040803	0.246641	3.4322656	0.03153925	0.069498	1.136046	0.651685	0.079223	0.819111	0.815461
	TNF	0.252698	0.776601	2.6658632	0.00299432	0.370601	0.713121	0.693592	1.728727	2.737404	N/A

Extended Data Table 4. Human interferon and cytokine genes upregulated during SARS-CoV-2 infection.

Transcripts per million (TPM). Log2 fold change (Log2FC) in TPM compared to naïve controls. P-values were calculated using

DESeq2 and adjusted for multiple testing using a False Discovery Rate. Not applicable (N/A): DESeq2 could not calculate a p-value

due to the variance between samples

Group	Mouse	Sex	Human Donor	Weeks Post-Surgery
Vehicle	47	M	F33	15
	48	M	F33	15
	49	F	L33	11
	50	F	L33	11
	51	M	T33	13
	52	M	T33	13
	53	M	T33	13
	54	M	T33	13
EIDD-2801	55	M	F33	15
	56	M	F33	15
	57	F	L33	11
	58	F	L33	11
	59	M	T33	13
	60	M	T33	13
	61	M	T33	13
	62	M	T33	13

Extended Data Table 5. Description of LoM used to evaluate the efficacy of EIDD-2801 pre-exposure prophylaxis.